

Interactions between Myosin and Actin Crosslinkers Control Cytokinesis Contractility Dynamics and Mechanics

Elizabeth M. Reichl,^{1,7} Yixin Ren,¹ Mary K. Morpew,⁵ Michael Delannoy,⁴ Janet C. Effler,^{1,6} Kristine D. Girard,¹ Srikanth Divi,¹ Pablo A. Iglesias,^{3,6} Scot C. Kuo,^{1,3,4} and Douglas N. Robinson^{1,2,*}

¹Department of Cell Biology

²Department of Pharmacology and Molecular Sciences

³Department of Biomedical Engineering

⁴The Institute for Biomedical Sciences Microscope Facility
Johns Hopkins University School of Medicine
Baltimore, Maryland 21205

⁵Boulder Laboratory for 3-D Electron Microscopy of Cells
University of Colorado

Boulder, Colorado 80309

⁶Department of Electrical and Computer Engineering
Johns Hopkins University
Baltimore, Maryland 21218

Summary

Introduction: Contractile networks are fundamental to many cellular functions, particularly cytokinesis and cell motility. Contractile networks depend on myosin-II mechanochromism to generate sliding force on the actin polymers. However, to be contractile, the networks must also be crosslinked by crosslinking proteins, and to change the shape of the cell, the network must be linked to the plasma membrane. Discerning how this integrated network operates is essential for understanding cytokinesis contractility and shape control. Here, we analyzed the cytoskeletal network that drives furrow ingression in *Dictyostelium*.

Results: We establish that the actin polymers are assembled into a meshwork and that myosin-II does not assemble into a discrete ring in the *Dictyostelium* cleavage furrow of adherent cells. We show that myosin-II generates regional mechanics by increasing cleavage furrow stiffness and slows furrow ingression during late cytokinesis as compared to *myoII* nulls. Actin crosslinkers dynactin and fimbrin similarly slow furrow ingression and contribute to cell mechanics in a myosin-II-dependent manner. By using FRAP, we show that the actin crosslinkers have slower kinetics in the cleavage furrow cortex than in the pole, that their kinetics differ between wild-type and *myoII* null cells, and that the protein dynamics of each crosslinker correlate with its impact on cortical mechanics.

Conclusions: These observations suggest that myosin-II along with actin crosslinkers establish local cortical tension and elasticity, allowing for contractility independent of a circumferential cytoskeletal array. Furthermore, myosin-II and actin crosslinkers may influence each other as they modulate the dynamics and mechanics of cell-shape change.

Introduction

Cytokinesis is one of the most elegant cellular shape changes, as a mother cell reforms into two daughter cells in as little as 5 min. Fundamentally mechanical, cytokinesis is driven by myosin-II and actin filaments, and signaling pathways emanating from the mitotic spindle ultimately lead to their accumulation along the equatorial region of the cell [1]. Myosin-II is a mechanoenzyme that uses the energy of ATP hydrolysis to move actin filaments. The actin filaments in combination with crosslinkers give cells their shape and mechanical properties. The actin crosslinking proteins stabilize actin filament interactions and tune the mechanical (rheological) properties of the actin network. Thus, the actin crosslinkers define the passive material properties of the network, whereas myosin-II uses energy to modify this network, creating an active network [2, 3]. Because of their central importance to cell function, how actin networks and myosin-II motors control the mechanical properties of cells is of considerable interest. Reconstitution systems have been developed to explore how actin networks respond to mechanical stress (force per area, pressure) and deformation (response of the network to mechanical stress) and how myosin-II contributes to active and passive properties of these actin networks [4–6]. However, it is unclear what the relevant mechanical properties of dividing cells are, how they are generated molecularly, and how they contribute to cytokinesis cell-shape change.

Classically, myosin-II is considered the primary force generator of cytokinesis, generating long-distance forces that deform the network. In this most general case, myosin-II pulls on dynamic actin filaments that are either crosslinked to other actin filaments or to the membrane, constricting the cleavage furrow cortex. In many, but not all, cell-types, these actin networks are further organized into concentric antiparallel arrays, allowing the myosin motors to pull the filaments, contracting the membrane in a purse-string fashion. However, neither *Dictyostelium* nor mammalian tissue culture cells require myosin-II for mitosis-coupled cell division if the cells are adherent, and recent studies have suggested other roles for myosin-II such as in removing actin filaments from the equatorial region during furrow constriction [7–9]. The actin crosslinking proteins link the filaments together so that when myosin-II pulls against the filament, tension on the filament can propagate into the crosslinked network. Even with this basic framework, it is not understood in any system how myosin-II and actin crosslinkers interact to contract the network nor how these factors control the dynamic features of furrow ingression. Also, because myosin-II pulls on filaments bound by the crosslinkers, the crosslinkers and myosin-II may modulate each other's activities. Finally, it is not understood how the cleavage furrows of wild-type cells constrict in such a stereotypical fashion nor how cleavage furrow ingression can occur without myosin-II.

To address these questions, we use the model system *Dictyostelium* to study cytokinesis cell-shape change. This organism performs cytokinesis in a similar fashion to many types of mammalian cell culture cells and is readily amenable to mechanical and genetic interaction studies. By using this system, we have discovered and are studying a two-module system of

*Correspondence: dnr@jhmi.edu

⁷Present address: Human Genome Sciences, Inc., 14200 Shady Grove Road, Rockville, Maryland 20850.

equatorial (myosin-II and the actin crosslinker cortexillin) and global/polar (RacE small GTPase and actin crosslinkers dynactin, coronin, enlazin, and fimbrin) proteins that form the genetic basis of the shape control system that regulates cytokinesis contractility (this paper) [10–13].

Here, we establish that the actin network in the contractile zone of *Dictyostelium* cells is a meshwork, rather than the circumferential actin ring found in many cell types. We then set out to uncover how actin and myosin-II interact to control cytokinesis contractility, using a variety of mechanical and dynamical approaches to study the contractile system. We conclude that during *Dictyostelium* cytokinesis, myosin-II generates a tension and stiffness differential between the furrow and polar cortex, that the dynamics of actin crosslinkers vary spatially during cytokinesis, and that these crosslinker dynamics are altered in *myoII* null cells. Because changes in cell mechanics are the logical output of regulatory pathways that provide the spatiotemporal control of cytokinesis, this analysis offers an analytical framework for ultimately linking these regulatory pathways to the mechanical changes that drive cytokinesis shape change.

Results

The Actin Network Is a Meshwork in the *Dictyostelium* Cleavage Furrow

By using transmission electron microscopy (Pt-TEM) and scanning electron microscopy (Pt-SEM), we determined that the actin polymer network is assembled into a meshwork in the furrow region of dividing *Dictyostelium* cells (Figure 1A and Figures S1A–S1C available online; see the Supplemental Experimental Procedures). In images of wild-type ($n = 73$) and *myoII* null ($n = 6$) dividing cells, we never observed a circumferential orientation of actin filaments at the equator; instead the filaments were assembled into a meshwork, similar to the cytoskeletons of interphase cells and polar cortices of dividing cells (Figures S1A, S1D, and S1E). Throughout cytokinesis the actin filament density at the furrow appeared to be nearly constant by Pt-TEM. We confirmed this by quantitative fluorescence imaging of rhodamine-phalloidin-stained cytoskeletons (Figure S1F). To complement the Pt-TEM and Pt-SEM, we used 3D-EM tomography (3D-EM) of plastic sections of plunge-frozen, freeze-substituted dividing cells, which also revealed a highly disordered actin filament network near the plasma membrane (Figure 1B, Figure S1G, and Movies S1–S4; see also the Supplemental Experimental Procedures) [14]. Because the IMOD software package used to build the 3D-EM tomograms allows one to recover the dimensions of each structure drawn, we were able to analyze the actin filament length distribution, which gave an average filament length of 94 ± 57 nm (mean \pm SD; Figure S1H). This compares well with the 200 nm mean length estimated previously for vegetative cells by using kinetic criteria [15]. From the filament length and number, and the bridge volume, we determined the concentration of F-actin in the late-stage intercellular bridge (Figure S1H) to be $150 \mu\text{M}$, which is reasonable considering the average polymeric actin concentration for vegetative cells is $70 \mu\text{M}$ [16].

For independent approaches, we used 3D-deconvolution (3D-decon) of rhodamine-phalloidin-stained fixed cells to view the actin distribution and 3D-decon and total-internal reflection fluorescence (TIRF) imaging of live cells expressing GFP-myosin-II to observe the myosin-II distribution (Figures 1C–1F). Neither actin nor myosin-II had a continuous ring

distribution at the equator by any method or at any stage of furrow ingression. Instead, the intensity of the actin and myosin-II was greatest at the lateral cortex of the furrow. This is especially apparent in the TIRF images in which the disorganized network of the myosin-II thick filaments had the highest concentration along the lateral edge of the cleavage furrow cortex. In later stages of furrow thinning, the bridge lifts from the surface and is not observable by TIRF microscopy. Birefringence imaging of dividing *Dictyostelium* cells compressed by a sheet of agarose had also revealed cytoskeletal filaments oriented both perpendicularly and parallel to the long axis of the furrow region [17]. Overall, there is no apparent uniform contractile ring of actin or myosin-II in the equator of dividing *Dictyostelium* cells grown on surfaces. Though many organisms use a concentric array of actin and myosin-II filaments (for example, see [18–20]), some cell-types, such as mammalian NRK and Swiss 3T3 cells, also have a more disordered actin and myosin-II network [21, 22], similar to what we observe in *Dictyostelium*.

More generally than a particular polymer organization, the deformation of living actin networks depends on two key features: actively generated forces from myosin-II and from actin polymer dynamics coupled with cell traction and the resistance to deformation (stiffness) from actin-crosslinking proteins. Because the actin filaments are very short in *Dictyostelium*, crosslinking proteins likely play an important role in linking the filaments together to form an integrated network. Cytokinesis cell-shape evolution may also depend on fluid dynamical features (similar to Laplace-like pressures that originate from surface tension and which minimize the surface area to volume ratios in liquids) from cortical tension through the crosslinked actin network that can help promote furrow ingression [13]. Therefore, to understand how the actin-myosin-II network contracts during cytokinesis, we dissected how myosin-II and actin crosslinkers control cytokinesis contractility dynamics and mechanics.

Role of Myosin-II during Cytokinesis

To assess how myosin-II impacts the dynamics and mechanics of cytokinesis contractility, we examined the morphology, dynamics, and mechanics of interphase and dividing cells with altered myosin-II mechanochemistry (Table S1). We previously predicted that wild-type furrowing occurred ~ 50 -fold more slowly than expected based solely on fluid dynamical considerations. Consistent with these predictions, we demonstrated that by removing the global proteins RacE and dynactin, thereby reducing the proposed resistive stresses, the furrow-thinning rates increased ~ 30 -fold compared to wild-type [13]. Additionally, a five-fold slower myosin (ΔBLCBS) that lacks light chain binding sites could rescue *myoII* null cytokinesis nearly to wild-type levels [23]. In this study, we examined cytokinesis of *myoII* null cells complemented with 10-fold slower motor, S456L, which moves slower due to a 3-fold longer ADP-bound time and one-fourth productive step-size [24]. This S456L motor expresses at wild-type levels but only rescues the growth rates in suspension culture to one-third of wild-type levels. However, the slower motor rescued the cytokinesis morphology and furrowing dynamics to wild-type levels on surfaces (Figure S2 and Movies S5–S7). Remarkably, the cleavage furrows from cells expressing wild-type or 10-fold slower myosin-IIs had indistinguishable furrow-thinning trajectories, whereas the *myoII* null cleavage furrows contracted faster late in furrow ingression than either of the strains with myosin-II, indicating that myosin-II actually slows late stage

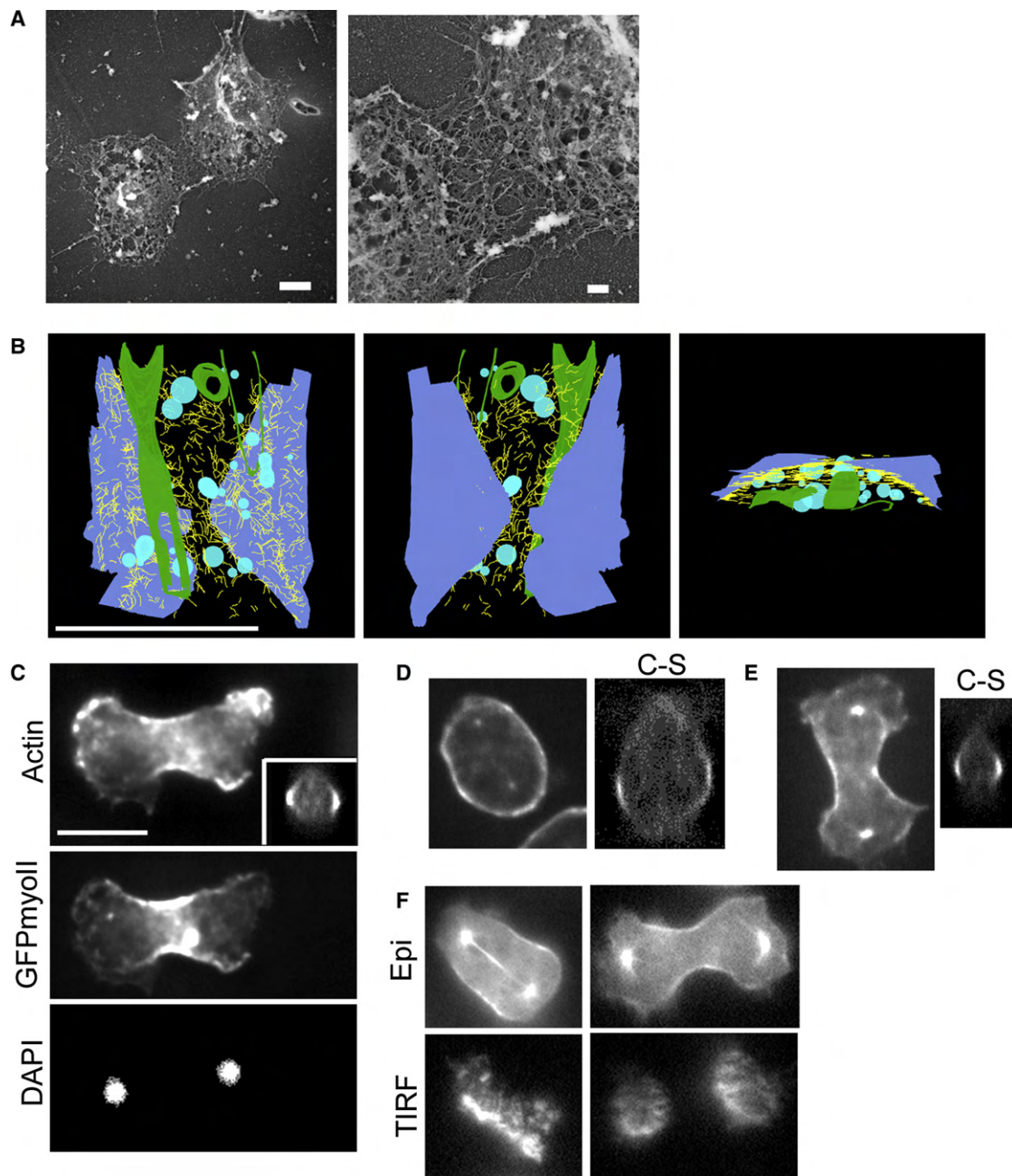


Figure 1. Organization of Actin Filaments and Myosin-II in the Cleavage Furrow Cortex of Adherent *Dictyostelium* Cells

Actin filaments are organized into a meshwork, and actin and myosin-II are not enriched in a uniform ring as revealed by platinum-shadowed transmission electron microscopy (Pt-TEM, [A]), 3D-electron tomography (3D-EM, [B]), 3D-deconvolution (3D-decon, [C-E]), and total internal reflection fluorescence (TIRF; [F], lower images) microscopy.

(A) The actin network is observed at the furrow of a wild-type cell by Pt-TEM. Scale bars, 2 μm and 500 nm.

(B) Rotated 3D-EM images of a model of a 0.5 μm section (derived from combining two adjacent sections) of the lower surface of a cleavage furrow reveal disordered actin filaments. Mitochondria are green, vesicles are cyan, plasma membrane is blue, and the actin filaments are yellow. The first two panels show the furrow model viewed from top and bottom, respectively. The third panel is the furrow viewed down the long axis of the furrow. Scale bar, 2 μm , applies to all panels. The Z series of the raw EM data can be found in [Movie S1](#). The corresponding movie of the model can be found at [Movie S2](#).

(C) Nonuniform cleavage furrow cortical actin. TRITC-phalloidin staining of filamentous actin in a wild-type cell. Inset shows a cross-section of the furrow actin where the actin is enriched along the lateral surface. Scale bar, 10 μm applies to all images. Equatorial localization of GFP-myosin-II and binucleation (DAPI) confirms cell was undergoing cytokinesis prior to fixation.

(D and E) Noncircumferential distribution of myosin-II thick filaments. Wild-type cells expressing GFP-tubulin and GFP-myosin-II reveal that, like actin, myosin-II does not form a continuous ring at the cleavage furrow. (D) Early-stage dividing cell. (E) Late-stage dividing cell. The “C-S” images show the cross-sectional fluorescence intensities of the furrow.

(F) Epifluorescence and TIRF images indicate that myosin-II is not circumferentially oriented at the basal region of the furrow. Note that at later stages of cytokinesis, the furrow lifts from the surface.

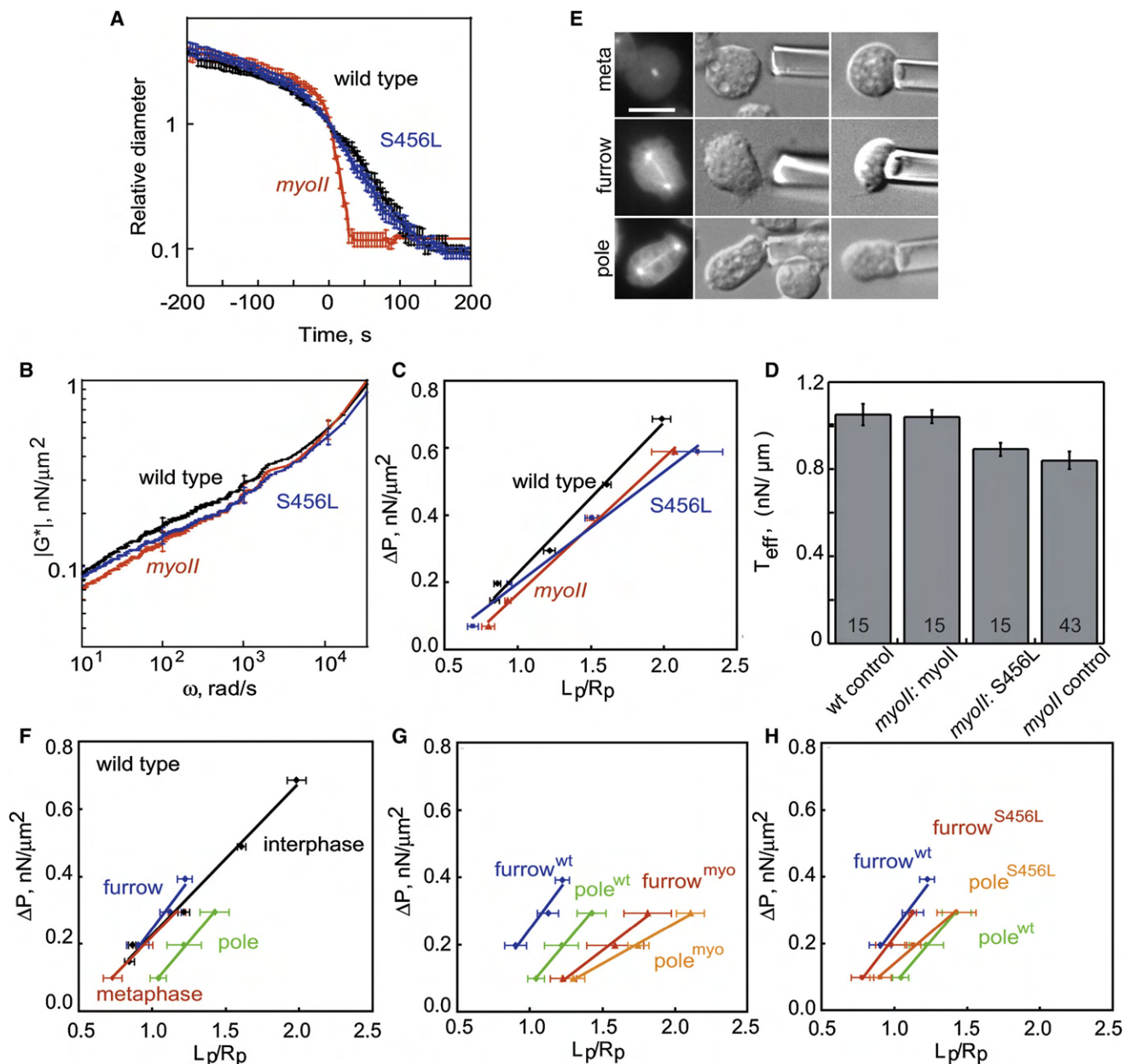


Figure 2. Wild-Type Myosin-II Mechanochemistry Is Required for Wild-Type Interphase Mechanics, but Not Cytokinesis Mechanics and Kinetics

(A) Comparison of furrow-thinning trajectories in cells expressing wild-type myosin-II or myosin-II S456L to *myoII* null cells shows that S456L is able to fully restore the uniform furrow-thinning kinetics of wild-type dividing cells. Note that *myoII* null cells have a faster furrow-thinning rate at later stages of division. (B–D) Expression of myosin-II S456L in *myoII* cells does not fully recover wild-type cellular mechanics during interphase. (B) *MyoII* cells have lower viscoelasticity ($|G^*|$) than wild-type cells as measured by LTM. (C and D) *MyoII* cells are more deformable (C) and have a lower effective cortical tension (D), as measured by MPA. The S456L cells have cortical mechanics similar to wild-type cells at longer time-scales (10^2 rad/s, [B]) and smaller deformations (lower L_p/R_p , [C]) but are more like *myoII* cells at shorter time-scales ($>10^2$ rad/s, [B]) and larger deformations (larger L_p/R_p , [C]). (E) Representative micrographs showing cells aspirated at metaphase and during cytokinesis at the pole and furrow. For the polar cortex, we aspirated at angles ranging from parallel to perpendicular to the spindle axis with no detectable differences in the level of deformability. (F) The degree of deformability of wild-type interphase and metaphase cells was not significantly different. During anaphase, the furrow was slightly less deformable than during metaphase, whereas the pole was more deformable than the furrow or metaphase cortices. (G) Conversely, the furrow and pole of *myoII* cells were not significantly different from each other and both regions were much more deformable than the polar region of wild-type cells. (H) S456L reduces the level of deformability of the furrow and polar regions to wild-type levels. Error bars indicate standard error of the mean. Sample sizes for (D) are shown on the histograms. Sample sizes for (A) are provided in Table S2; sample sizes for (B) are shown in the histograms in Figure S3, and the calculated E values and sample sizes for (C) and (F)–(H) are provided in Table S3.

furrow ingression (Figure 2A and Table S2). Thus, the velocity of the motor is clearly not rate limiting, and other processes must govern the furrow ingression rate (see below).

To determine how myosin-II contributes to cell deformability (a stiffer material is less deformable), we used two methods: laser-tracking microrheology (LTM) and micropipette

aspiration (MPA). These methods draw upon very different principles and assumptions, but used in combination, they allow for crosscomparison and for different features of cortex mechanics to be assessed. In LTM, the surface-attached bead particles serve as noninvasive reporters of cortical stiffness (measured as complex viscoelastic moduli (G^*)); see the [Experimental Procedures](#)), which is important because myosin-II has load-dependent actin binding that can alter the enzyme's duty ratio [25–27]. From LTM, phase-angle information also can be extracted to relate the solid- to liquid-like properties of the cortex (see the [Experimental Procedures](#)). However, slow Brownian motions (on timescales >200 ms) of particles are obscured by active force generation in the cell, limiting LTM's usefulness for measuring viscoelastic moduli to time scales ≤ 100 ms [3]. Furthermore, it has not been feasible to apply LTM to dividing cells in a statistically rigorous manner. In contrast, MPA measures mechanics on longer time scales but requires relatively large mechanical strains for the measurements to be made. MPA offers the ability to position micropipettes so that spatial mechanics can be assessed for cytokinetic cells ([Figure 2E](#)). On the longest 100 ms time scale (10 rad/s) measured by LTM, the interphase cortex of wild-type cells have a viscoelastic modulus (G^*) of $0.1 \text{ nN}/\mu\text{m}^2$ (100 Pa), which from the power-law behavior might extrapolate to $\sim 0.07 \text{ nN}/\mu\text{m}^2$ at 1 s ([Figure 2B](#)). Because the beads are surface attached and may not be fully immersed in the network, this could be an underestimation of the viscoelastic modulus of the cortex. Yet, these LTM values agree well with the elastic modulus (E) of $0.1 \text{ nN}/\mu\text{m}^2$ obtained from the ΔP versus L_p/R_p relationship measured by MPA ([Figure 2C](#) and [Table S3](#); also see the [Experimental Procedures](#)). When the cells are more spherical, as during interphase, MPA can also be used in a different way to measure an effective cortical tension (T_{eff}) (measured at $L_p/R_p = 1$), which was $1 \text{ nN}/\mu\text{m}$ for wild-type cells ([Figure 2D](#); see the [Supplemental Experimental Procedures](#)) [10]. Thus, the combination of these methods allows three parameters to be assessed: a frequency-dependent viscoelastic modulus with its phase angle (LTM), an effective cortical tension (MPA), and an elastic modulus (MPA). However, for some of the different genetic mutants and in some of the different cell cycle phases, the plots of ΔP versus L_p/R_p have similar slopes but are offset (for example, wild-type versus *myoII* in [Figure 2C](#)). The offsets are likely due to nonlinearities of the cells' responses to small versus large deformations. As a result, we primarily interpret these data in terms of how the cell deforms in response to applied pressure (greater L_p/R_p at a given pressure implies greater deformability). Nevertheless, the calculated elastic moduli for each case are presented in [Table S3](#).

We first analyzed interphase wild-type, *myoII* null, and S456L cells by using LTM and MPA ([Figures 2B–2D](#) and [Figure S3](#)). By LTM, the *myoII* null cells had slightly lower viscoelastic moduli than the wild-type cells across all frequencies whereas the S456L mutant cells were lower than wild-type at high frequencies and comparable to wild-type at low frequencies ([Figure 2B](#) and [Figure S3](#)). In the frequency range of the LTM measurements, all strains measured here were more solid-like (phase angle values at 100 rad/s were 13° – 15° for all strains except for S456L, which had a phase angle of 11° ; see the [Experimental Procedures](#)). By MPA, the *myoII* nulls were more deformable than the wild-type cells and again the S456L mutant was intermediate between the two strains ([Figure 2C](#) and [Table S3](#)). The effective cortical tension was $\sim 20\%$ reduced for *myoII* null (which is similar to the 30%

reduction observed by needle poking [28]) and S456L cells when compared to wild-type control cells ([Figure 2D](#)). Thus, consistent with its significant (10-fold) motility defect, S456L only partially rescues the *myoII* null interphase mechanical defect.

During mitosis ([Figures 2E](#) and [2F](#); [Table S3](#)), wild-type metaphase cells were indistinguishable from interphase cells. However, as predicted by classical models, the polar cortex became much more deformable (polar relaxation [29, 30]) whereas the equator stiffened slightly (equatorial stimulation [31, 32]) during anaphase as compared to interphase cells ([Figure 2F](#)). In *myoII* null cells, the equatorial and polar cortices were not significantly different from each other but were significantly more deformable overall than wild-type cells ([Figure 2G](#) and [Table S3](#)). Perhaps explaining the similarity between wild-type and S456L furrowing dynamics, S456L rescued the deformability of the equatorial and polar cortices to wild-type levels ([Figure 2H](#) and [Table S3](#)). Therefore, the slowly decreasing furrow diameters of wild-type and S456L cells correlate with decreased deformability of the cleavage furrow cortex ([Figure 2A](#) versus [Figures 2F–2H](#)). S456L may provide more wild-type function in the context of the cleavage furrow cortex where myosin-II becomes enriched and where the cortex is actively deforming (straining), which may put the myosin-II under greater mechanical load. It should be noted that we recently documented mechanosensory responses in dividing cells, which occur on timescales of ~ 40 s after mechanical perturbation [33]. For the analysis presented here, we measured all genotypes within ~ 20 s of manipulation, and we also followed GFP-myosin-II in the rescued *myoII* null (*myoII*: GFPmyoII) cells to make sure that we did not trigger mechanosensory responses in the timeframe of the experiment. Therefore, these data reflect the level of deformability of the cortex, not mechanosensory responses.

Complex Interaction of Myosin-II and Crosslinkers in the Actin Network

To prevent nonproductive filament sliding, myosin-II requires crosslinking proteins to couple short filaments to each other so that the network deforms as a whole. Therefore, the actin crosslinkers represent the other half of the contractile system. Two classes of crosslinkers (global and equatorial) have been uncovered through genetic interaction screens [10, 11]. Cortillin-1 is an equatorially enriched actin crosslinker with membrane binding sites that are involved in *Dictyostelium* cytokinesis contractility and cortical mechanics [25, 34]. Globally distributed dynacortin has emerged as an important component that contributes to cytokinesis furrowing dynamics by acting as a brake to slow furrow ingression [11, 13]. Because dynacortin overexpression produces enlarged, multinucleated cells ([Figure S4A](#)) [11], we used this phenotype to screen for other factors that may act in the global pathway. We expressed a cDNA library in *Dictyostelium* cells and isolated the actin crosslinker fimbrin as a factor that produced enlarged, multinucleated cells that saturated at lower cell densities when overexpressed ([Figure S4A–S4C](#)). Similar to dynacortin, fimbrin is a globally distributed actin crosslinking and bundling protein ([Figure S4D](#)) [11]. Both dynacortin and fimbrin have similar apparent affinities for actin (K_d , $\sim 1 \mu\text{M}$) and cellular concentrations ($\sim 1 \mu\text{M}$), and increase cortical tension when overexpressed ([Figure S5](#)) [25, 35, 36].

Using LTM and MPA, we measured and compared the frequency spectra of viscoelastic moduli and cortical tensions of wild-type and *myoII* null cells devoid of these crosslinkers.

Interphase cells lacking myosin-II or dynacortin have lower viscoelastic moduli and cortical tension than control cells (Figures 3A and 3B and Figure S3). In contrast, *fimbrin* mutant cells have lower viscoelastic moduli than wild-type cells when measured by LTM, which measures fast time scales (ST, $p < 0.02$ at 10 and 100 rad/s; Figure 3C and Figure S3), but have similar cortical tension, which is measured on longer time-scales, to wild-type cells (ST, $p = 0.5$; Figure 3D). However, removal of fimbrin from *myoII* null cells did lead to a significant reduction in cortical tension, suggesting that myosin-II might modulate fimbrin's contribution to long time scale cortical mechanics (MPA) (ST, $p = 0.002$) (Figure 3D). Similarly, the differing contributions of dynacortin and fimbrin to cellular-scale mechanics may be observed in the furrow-thinning rates: *myoII* null cells lacking dynacortin thin faster than *myoII* null cells lacking fimbrin (Figure 3E and Table S2).

The mechanical properties of crosslinked actin networks are derived from the complex organization of the actin polymers and the kinetic properties of the crosslinking proteins [4, 37]. The organizational features lead to the structures and level of filament entanglements that define the mechanics of the network. The crosslinking proteins organize the structures and stabilize the entanglements: slower (longer lived) crosslinkers maintain stable associations between the polymers whereas faster crosslinkers release quickly, allowing the filaments to slide past one another (see the Discussion section). At the whole-cell level, discerning quantitatively the subtle differences in network organization is not yet feasible. However, we could begin to discern some of the kinetic features of the crosslinkers in wild-type and *myoII* null cells by using fluorescence recovery after photobleaching (FRAP) analysis.

First, we measured the dynamics of the crosslinkers and myosin-II in wild-type interphase cells. The fluorescence recovery rate of GFP-fimbrin ($\tau_{\text{rec}} = 0.26$ s) was faster than the rate for GFP-dynacortin ($\tau_{\text{rec}} = 0.45$ s; MW, $p = 1 \times 10^{-5}$). Overall, both were slower than soluble GFP in the cortical region of the cell (Table 1 and Figure S6). GFP-fimbrin and GFP-dynacortin also showed similar immobile fractions (Table 1 and Figure S7). In contrast, cortexillin-I ($\tau_{\text{rec}} = 3.3$ s) and myosin-II ($\tau_{\text{rec}} = 8-10$ s) had similar immobile fractions but had significantly longer median recovery times than either fimbrin or dynacortin (Table 1 and Figures S6 and S7). Thus, a simple paradigm of fast global proteins and slow equatorial proteins is suggested from the interphase protein dynamics.

Next, we compared the dynamics of these crosslinkers in interphase wild-type and *myoII* null cells. Because fimbrin had a detectable impact on the cortical tension of *myoII* null cells, but not wild-type cells, whereas dynacortin had its greatest impact on the viscoelastic moduli and cortical tension of wild-type cells, we wondered if these two crosslinkers would have differential dynamics in wild-type and *myoII* null cells. Indeed, fimbrin's τ_{rec} was faster in wild-type cells (0.26 s) than in *myoII* null cells (0.68 s) (MW, $p = 1 \times 10^{-7}$; Table 1 and Figure S6), correlating with its impact on *myoII* null cortical tension. However, dynacortin was slower in wild-type cells (0.45 s) than in *myoII* null cells (0.29 s) (MW, $p = 0.005$). In contrast, cortexillin-I showed only a weakly significant increase in τ_{rec} (MW: $p = 0.04$) but a larger immobile fraction without myosin-II (MW, $p = 0.006$; Table 1; and Figures S6 and S7).

Finally, we compared the dynamics of these proteins during wild-type cytokinesis. The τ_{rec} of both GFP-fimbrin and GFP-dynacortin increased at the equatorial region to 0.58 s (MW, $p = 0.006$) and 0.98 s (MW, $p = 0.005$), respectively, whereas the recovery times at the polar cortices remained at

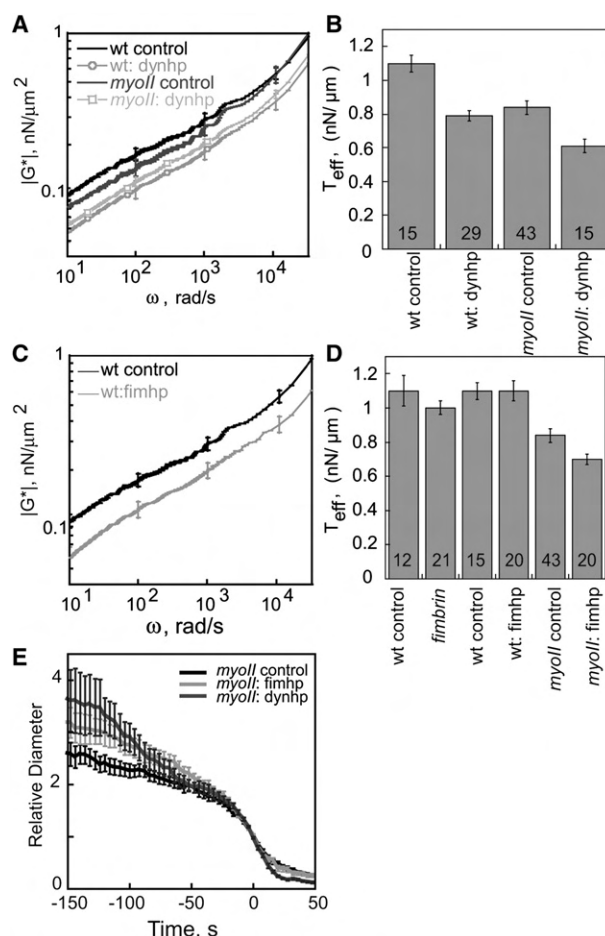


Figure 3. Dynacortin Has a Greater Contribution to Cortical Mechanics and Furrow-Thinning Kinetics Compared to Fimbrin

(A) Removal of dynacortin and/or myosin-II reduces the viscoelasticity (G^*) of interphase cells as measured by LTM. (B) Likewise, myosin-II and dynacortin contribute to the effective tension (T_{eff}) as measured by MPA. (C) Removal of fimbrin reduces the viscoelasticity (G^*) of interphase cells as measured by LTM. (D) In wild-type cells, fimbrin does not contribute to cortical tension as measured by MPA, but it does contribute significantly in a *myoII* null background. Both the *fimbrin* knockout strain (*fimbrin*) and *fimbrin* RNAi (*fimhp*) strains have the same effects. The control for *fimbrin* is the parental strain and the control cells for the *fimhp*-expressing cells are wild-type cells carrying the empty vector. (E) In a *myoII* null background in which fimbrin has a significant mechanical contribution on longer time-scales (MPA), reduction of fimbrin or dynacortin increases the rate of furrow ingression compared to control cytokinesis. However, dynacortin has a greater contribution to the furrow-thinning kinetics than fimbrin has. Error bars represent the standard error of the mean.

interphase levels (Table 1 and Figure S6). GFP-cortexillin-I had a recovery time that was similar between the equator ($\tau_{\text{rec}} = 5.4$ s) and pole ($\tau_{\text{rec}} = 4.5$ s) (MW, $p = 0.7$) (Table 1 and Figure S6), whereas its immobile fraction increased during cytokinesis (MW, $p = 0.038$) (Table 1 and Figure S7). Overall, each of the crosslinkers in the equatorial region has a longer lifetime, whereas those in the polar region have shorter lifetimes. In sum, for these proteins, a simple paradigm of slow equatorial and fast global crosslinking proteins appears to control cytokinesis shape change.

Table 1. Median Recovery Times, τ_{rec} , and Median Immobile Fractions, F_i , for Global Class and Equatorial Class Proteins in Interphase and during Cytokinesis: FRAP Analysis

	τ_{rec}, F_i (n)			
	Interphase		Cytokinesis	
	Wild-type	<i>myoII</i>	Equator	Pole
Global Class				
GFP-dynacortin	0.45 s, 26% (24)	0.29 s, 40% (30)	0.98 s, 31% (21)	0.51 s, 38% (19)
GFP-fimbrin	0.26 s, 33% (30)	0.68 s, 41% (46)	0.58 s, 2.9% (13)	0.31 s, 21% (16)
Equatorial Class				
GFP-cortexillin-I	3.3 s, 32% (33)	5.4 s, 49% (42)	5.4 s, 57% (14)	4.5 s, 53% (13)
GFP-myosin-II	11 s*	7.6 s, 24% (8)	10 s*	
Soluble				
GFP (cortex)	0.15 s, 13% (14)			

*Values from [48]. Mean \pm SEM are shown on the histograms in Figures S6 and S7.

Discussion

Because cytokinesis is an inherently mechanical process, mechanical studies have played an important role in cytokinesis research for many decades (for example, see [29, 32, 38, 39]). From these studies, a diversity of mechanical scenarios for cytokinesis contractility has been observed across a wide range of organisms. However, more fundamentally, the contractility of a cytoskeletal network results from the integrated behavior of actin crosslinkers and myosin-II. Our data demonstrate that myosin-II and global and equatorial actin crosslinking control spatial mechanics in the absence of a clear concentric ring of actin polymers (Figure 4). In dividing wild-type cells, the polar cortex is more deformable than the equatorial cortex, and the globally distributed actin crosslinkers have much shorter recovery times than the equatorial crosslinkers. The correlation between crosslinker lifetimes and cortex deformability suggests that myosin-II and equatorial crosslinkers primarily increase the local cortical tension and elasticity in the furrow region. This increased equatorial cortical tension may generate surface stresses that lead to Laplace-like pressures, which help push cytoplasm out of the furrow region. The Laplace-like pressures may originate from stresses in the actin network that are actively generated by pulling forces from myosin-II and/or from pushing forces from actin assembly at the

poles. Because the cells are highly elastic (phase angle $\sim 15^\circ$ at 100 rad/s), mechanical stresses may propagate through the crosslinked network. However, the cell cortex and cytoplasm have enough viscous character that as the pole-to-pole length increases and the furrow radius decreases, the surface stresses squeeze cytoplasm from the midzone, driving furrow ingression in a manner analogous to how a fluid droplet breaks up. Wild-type furrows also may constrict more slowly than *myoII* null furrows during late cytokinesis stages because of their increased elasticity, which may lead to a longer elastic relaxation time (previously estimated to be ~ 30 s for wild-type cells [13]). In contrast, the higher level of deformability of dividing *myoII* null cells may facilitate their ability to divide with the aid of traction. In the *myoII* nulls, force generation from actin assembly at the poles likely allows the emerging daughter cells to crawl apart enough to form the appropriate geometry for equatorial cortical stresses to promote the Laplace-like pressures in the furrow region [10, 13, 40, 41]. Importantly, *myoII* null cells do not elongate enough to simply crawl apart; rather, cytoplasm flows from the midzone and the furrowing dynamics of the *myoII* null cells can be modeled as a surface tension-driven process, further supporting a role for the Laplace-like pressures [13].

Although many types of cells perform cytokinesis through the constriction of a purse-string of actin and myosin-II

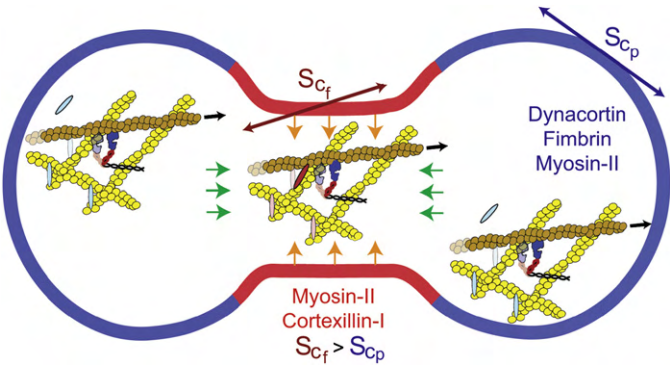


Figure 4. Model for Cytokinesis Cell-Shape Change through the Contraction of an Actin Meshwork

Here, myosin-II and actin crosslinkers interact to control furrow ingression dynamics, equatorial and polar cortical tension, and crosslinker lifetimes. The equatorial cortex is principally controlled by myosin-II and cortexillin, whereas the global/polar cortex is modulated by dynacortin, fimbrin, and myosin-II. The local increased cortical tension ($S_{cf} > S_{cp}$) by myosin-II generates equatorial stresses (orange arrows) that help squeeze cytoplasm from the furrow region, whereas the globally distributed crosslinkers generate resistive stresses (green arrows) that slow furrow ingression (this paper and [13]). The equatorial crosslinker cortexillin-I and equatorial populations of fimbrin and dynacortin (represented as red ellipses) persist much longer at the cortex, perhaps contributing to the increased tension in this region. Conversely, polar actin crosslinkers (fimbrin and dynacortin represented as blue ellipses) release from the network on fast time scales, making the global cortex more deformable. This system of myosin-II and equatorial and global actin crosslinkers generates the stress differential that drives and controls the dynamics of cytokinesis cell-shape change.

filaments, mammalian NRK cells, Swiss 3T3 cells, and *Dictyostelium* cells do not have such a highly organized structure of concentric actin filaments (this paper) [21, 22]. Despite these structural variations, how myosin-II, actin polymers, and actin crosslinkers interact is likely to be a fundamental principle, governing cytokinesis contractility dynamics. Indeed, α -actinin functions in mammalian NRK cells analogously to the actin crosslinkers studied here: NRK cells devoid of α -actinin have accelerated furrow ingression, similar to *dynacortin* and *fimbrin* mutants, and myosin-II inhibition leads to slower α -actinin dynamics, similar to *fimbrin* [42].

To deform the cytoskeletal network, myosin-II motor proteins must pull on actin filaments that are crosslinked by crosslinking proteins, and without crosslinkers, myosin-II would simply slide filaments past one another without deforming the network [43]. Therefore, interactions between the crosslinkers and motors are an essential feature of a contractile system, and the crosslinkers and motors are poised to influence each others' activities through crosstalk across the filaments. This crosstalk may occur principally in three ways: (1) through structural organization of the filament network, (2) through binding interactions (allostery) through the actin filament, and/or (3) through tension effects across the filaments. Structurally, the crosslinker or myosin-II may organize filaments into network structures that affect the binding of the other. By binding, the motor or crosslinker could alter the conformation of the actin filament so that it modulates the binding of the other. Finally, because myosin-II pulls on the actin filament, tension through the filament may stabilize or destabilize the binding of the crosslinker. Whether tension directly influences the crosslinker binding dynamics, slow crosslinkers would not only make the network less deformable (more elastic, increased stiffness) but would provide the mechanical load needed for myosin-II to generate tension on the network.

Cortexillin-I appears to have an important role in assisting myosin-II in tension generation. Cortexillin-I is enriched in the furrow cortex and with its slow recovery dynamics (~10-fold slower than those of *dynacortin* and *fimbrin*), it is likely to be the major crosslinker that myosin-II pulls against to generate increased cortical tension and elasticity in the furrow region. From other work, cortexillin-I and myosin-II relocate to sites of cell deformation in dividing cells as part of a mechanosensory cell-shape control system, whereas *dynacortin* and *fimbrin* do not [33]. *Cortexillin-I* mutants also have a similar reduction in cortical stiffness and have a slower initial phase of furrow ingression similar to *myoII* null cells [10, 13, 25]. All of these observations together identify cortexillin-I and myosin-II as core components of a contractile module that controls cytokinesis cell-shape change.

In contrast, *fimbrin* and *dynacortin* might antagonize myosin-II. Both proteins provide a braking function, slowing furrow ingression kinetics, and both have fast (subsecond) recovery dynamics in the cortex. In vitro, myosin-II can extract actin filaments from *fimbrin* crosslinked networks, suggesting that myosin-II pulling might release *fimbrin* crosslinking [36]. Similarly, in our study, removal of *fimbrin* from a *myoII* null, but not from wild-type, led to a significant reduction in cortical tension, suggesting that myosin-II may antagonize *fimbrin*'s crosslinking activity. Alternatively, *dynacortin* has slower recovery dynamics in wild-type cells than in *myoII* null cells and has a bigger impact on the viscoelastic moduli and cortical tension of wild-type cells than *myoII* null cells. Precedence exists for crosslinkers to have slower dynamics in response to myosin-

II-generated forces, as has been suggested for *zyxin* at the focal adhesion [44].

Overall, complex interactions between actin-associated proteins control cytokinesis dynamics and mechanics, and to decipher this complexity requires quantitative analysis of single and double mutant combinations of cytoskeletal and regulatory factors. As judged from latrunculin-treated cells, the cortical cytoskeleton contributes ~90% of the cortical stiffness [25]; yet myosin-II and each individual crosslinking protein only contributes ~20%–30% to cortical tension (this paper) [10]. However, single versus double mutant combinations of myosin-II or cortexillin-I with global crosslinkers do not necessarily lead to additive reductions in cortical stiffness and tension (this paper) [25]. Therefore, the molecular determinants of cortical mechanics interact in a highly complex fashion, leading to nonlinear effects. Although one can only speculate as to how many crosslinkers have to be removed to reduce tension to the latrunculin level, the small GTPase *RacE* may provide part of the clue. *RacE* nulls have a 70%–80% reduction in cortical tension [45], and *RacE* is known to be required for the accumulation of crosslinkers *dynacortin* and *coronin*, but not *fimbrin* or *enlazin*, at the cortex [11]. Thus, cytokinesis shape change is the result of a complex system of interacting regulatory and cytoskeletal proteins that control cell mechanics.

In sum, with our current data sets (this paper) [10, 13, 25], we are building an analytical framework that relates contractility dynamics, cell mechanics, and crosslinker recovery dynamics. This framework provides a number of quantitative outputs that can be assessed to see how cytokinesis regulatory pathways modulate cytokinesis cell-shape change. Ultimately, it will be important to develop the computational tools to test this analytical framework quantitatively. Additionally, whole-cell measurements always have the caveat that unknown proteins may impact the system. Therefore, the development of reconstitution systems that allow the interface between mechanical strain, crosslinked actin network structure, and crosslinker dynamics to be directly analyzed and contrasted with these in vivo data will be essential.

Experimental Procedures

Details of the cell strains, genetic screening, analysis of growth rates, molecular biology techniques, Pt-TEM, 3D-EM tomography, 3D-deconvolution and TIRF fluorescence imaging, and FRAP and FLIP analyses can be found online in the [Supplemental Data](#).

Furrow-Thinning Dynamics

Time-lapse DIC images were taken at 2 s intervals with a 40 \times (N.A. 1.3) objective with 1.6 \times optovar. Minimal furrow diameters and lengths were measured with 4 s time resolution, and furrow-thinning dynamics (FTDs) were analyzed by using a previously described rescaling strategy [13].

Laser-Tracking Microrheology

Laser-tracking microrheology (LTM) of interphase cells was performed by using previously published methods [25]. In short, beads were tracked for 11 s iterations. The generalized Stokes-Einstein relationship is used to convert bead fluctuations into cell viscoelasticity spectra:

$$|G^*| = \frac{2K_B T}{6\pi r \langle msd \rangle}, \quad (1)$$

where r equals the bead radius, which is 0.35 μ m. $|G^*|$ is a complex modulus that is a combination of elastic (storage) and viscous (loss) moduli so that $G^* = G' + iG''$. The phase angle (δ) relates these two components so that $G' = |G^*|\cos\delta$ and $G'' = |G^*|\sin\delta$. Lognormal means and standard error of the means of $|G^*|$ values are presented after transformation back into real space values.

Micropipette Aspiration

Micropipette aspiration (MPA) of logarithmically growing cells was performed by using glass pipettes with inner radii of 2.5–5 μm . DIC images were taken every 5 s with a 60 \times (NA 1.45) objective with 1.6 \times optivar. With MPA, different cell mechanical models such as solid-body deformation and the cortical shell-liquid core are used to convert the pressure-deformation relationships into mechanical parameters [46, 47]. The effective tension of interphase cells was measured at a pressure that induced a hemispherical deformation ($L_p/R_p = 1$) of the cell into the pipette. The tension was calculated using the Law of Laplace [47]:

$$\Delta P = 2T_{\text{eff}} \left(\frac{1}{R_p} - \frac{1}{R_c} \right). \quad (2)$$

To determine the relative stiffness of mitotic cells during metaphase and at the equator and poles during anaphase, pressure jumps using MPA were applied to the cells. The measurements were taken within 20 s of aspiration, and GFP-myosin-II was monitored to ensure that pressures were recorded prior to the mechanosensory response [33]. From the slope (m) of the ΔP versus L_p/R_p curves, the elastic modulus E could be estimated using the following equation:

$$E = \frac{3m}{2\pi\phi}, \quad (3)$$

where $\phi = 2.1$ [46].

Statistical Analyses

For each comparison, either a Mann-Whitney (MW) or two-tailed Student's t test (ST) was performed, and each p value has either MW or ST to designate the test used.

Supplemental Data

Supplemental Experimental Procedures, seven figures, and three tables are available at <http://www.current-biology.com/cgi/content/full/18/7/471/DC1/>.

Acknowledgments

We thank Ron Rock (University of Chicago), Nir Gov (Weizmann Institute), Tom Pollard (Yale University), Yu-li Wang (University of Massachusetts), and Alexandra Surcel for helpful suggestions on the manuscript. We thank Guenther Gerisch for mouse hybridomas expressing α -fimbrin antibodies and the *Dictyostelium* stock center for the *fimbrin* knockout and parental AX2-214 cells. This work was supported by National Institutes of Health grants GM066817 (to D.N.R.), GM071920 (to P.A.I.), GM59285 (to S.C.K.), and RR00592 (to Andreas Hoenger) and a National Science Foundation grant CCF 0621740 (to P.A.I. and D.N.R.).

Received: November 12, 2007

Revised: February 18, 2008

Accepted: February 19, 2008

Published online: March 27, 2008

References

1. Glotzer, M. (2005). The molecular requirements for cytokinesis. *Science* 307, 1735–1739.
2. Lau, A.W.C., Hoffman, B.D., Davies, A., Crocker, J.C., and Lubensky, T.C. (2003). Microrheology, stress fluctuations, and active behavior of living cells. *Phys. Rev. Lett.* 91, 198101.
3. Girard, K.D., Kuo, S.C., and Robinson, D.N. (2006). *Dictyostelium* myosin-II mechanochemistry promotes active behavior of the cortex on long time-scales. *Proc. Natl. Acad. Sci. USA* 103, 2103–2108.
4. Gardel, M.L., Shin, J.H., MacKintosh, F.C., Mahadevan, L., Matsudaira, P., and Weitz, D.A. (2004). Elastic behavior of cross-linked and bundled actin networks. *Science* 304, 1301–1305.
5. Mizuno, D., Tardin, C., Schmidt, C.F., and MacKintosh, F.C. (2007). Non-equilibrium mechanics of active cytoskeletal networks. *Science* 315, 370–373.
6. Chaudhuri, O., Parekh, S.H., and Fletcher, D.A. (2007). Reversible stress softening of actin networks. *Nature* 445, 295–298.
7. De Lozanne, A., and Spudich, J.A. (1987). Disruption of the *Dictyostelium* myosin heavy chain gene by homologous recombination. *Science* 236, 1086–1091.
8. Kanada, M., Nagasaki, A., and Uyeda, T.Q. (2005). Adhesion-dependent and contractile ring-independent equatorial furrowing during cytokinesis in mammalian cells. *Mol. Biol. Cell* 16, 3865–3872.
9. Murthy, K., and Wadsworth, P. (2005). Myosin-II-dependent localization and dynamics of F-actin during cytokinesis. *Curr. Biol.* 15, 724–731.
10. Octaviani, E., Effler, J.C., and Robinson, D.N. (2006). Enlazin, a natural fusion of two classes of canonical cytoskeletal proteins, contributes to cytokinesis dynamics. *Mol. Biol. Cell* 17, 5275–5286.
11. Robinson, D.N., and Spudich, J.A. (2000). Dynacortin, a genetic link between equatorial contractility and global shape control discovered by library complementation of a *Dictyostelium discoideum* cytokinesis mutant. *J. Cell Biol.* 150, 823–838.
12. Reichl, E.M., Effler, J.C., and Robinson, D.N. (2005). The stress and strain of cytokinesis. *Trends Cell Biol.* 15, 200–206.
13. Zhang, W., and Robinson, D.N. (2005). Balance of actively generated contractile and resistive forces controls cytokinesis dynamics. *Proc. Natl. Acad. Sci. USA* 102, 7186–7191.
14. Mastronarde, D.N. (1997). Dual-axis tomography: An approach with alignment methods that preserve resolution. *J. Struct. Biol.* 120, 343–352.
15. Podolski, J.L., and Steck, T.L. (1990). Length distribution of F-actin in *Dictyostelium discoideum*. *J. Biol. Chem.* 265, 1312–1318.
16. Haugwitz, M., Noegel, A.A., Karakesisoglou, J., and Schleicher, M. (1994). *Dictyostelium* amoebae that lack G-actin-sequestering profilins show defects in F-actin content, cytokinesis, and development. *Cell* 79, 303–314.
17. Fukui, Y., and Inoué, S. (1991). Cell division in *Dictyostelium* with special emphasis on actomyosin organization in cytokinesis. *Cell Motil. Cytoskeleton* 18, 41–54.
18. Kamasaki, T., Osumi, M., and Mabuchi, I. (2007). Three-dimensional arrangement of F-actin in the contractile ring of fission yeast. *J. Cell Biol.* 178, 765–771.
19. Maupin, P., and Pollard, T.D. (1986). Arrangement of actin filaments and myosin-like filaments in the contractile ring and of actin-like filaments in the mitotic spindle of dividing HeLa cells. *J. Ultrastruct. Mol. Struct. Res.* 94, 92–103.
20. Schroeder, T.E. (1973). Actin in dividing cells: Contractile ring filaments bind heavy meromyosin. *Proc. Natl. Acad. Sci. USA* 70, 1688–1692.
21. Fishkind, D.J., and Wang, Y.-L. (1993). Orientation and three-dimensional organization of actin filaments in dividing cultured cells. *J. Cell Biol.* 123, 837–848.
22. DeBiasio, R.L., LaRocca, G.M., Post, P.L., and Taylor, D.L. (1996). Myosin II transport, organization, and phosphorylation: Evidence for cortical flow/solution-contraction coupling during cytokinesis and cell locomotion. *Mol. Biol. Cell* 7, 1259–1282.
23. Zang, J.-H., Cavet, G., Sabry, J.H., Wagner, P., Moores, S.L., and Spudich, J.A. (1997). On the role of myosin-II in cytokinesis: Division of *Dictyostelium* cells under adhesive and nonadhesive conditions. *Mol. Biol. Cell* 8, 2617–2629.
24. Murphy, C.T., Rock, R.S., and Spudich, J.A. (2001). A myosin II mutation uncouples ATPase activity from motility and shortens step size. *Nat. Cell Biol.* 3, 311–315.
25. Girard, K.D., Chaney, C., Delannoy, M., Kuo, S.C., and Robinson, D.N. (2004). Dynacortin contributes to cortical viscoelasticity and helps define the shape changes of cytokinesis. *EMBO J.* 23, 1536–1546.
26. Yamada, S., Wirtz, D., and Kuo, S.C. (2000). Mechanics of living cells measured by laser tracking microrheology. *Biophys. J.* 78, 1736–1747.
27. Veigel, C., Molloy, J.E., Schmitz, S., and Kendrick-Jones, J. (2003). Load-dependent kinetics of force production by smooth muscle myosin measured with optical tweezers. *Nat. Cell Biol.* 5, 980–986.
28. Pasternak, C., Spudich, J.A., and Elson, E.L. (1989). Capping of surface receptors and concomitant cortical tension are generated by conventional myosin. *Nature* 341, 549–551.
29. Wolpert, L. (1966). The mechanical properties of the membrane of the sea urchin egg during cleavage. *Exp. Cell Res.* 41, 385–396.
30. White, J.G., and Borisy, G.G. (1983). On the mechanisms of cytokinesis in animal cells. *J. Theor. Biol.* 101, 289–316.
31. Rappaport, R. (1996). *Cytokinesis in Animal Cells* (Cambridge, U.K.: Cambridge University Press).

32. Matzke, R., Jacobson, K., and Radmacher, M. (2001). Direct, high-resolution measurement of furrow stiffening during division of adherent cells. *Nat. Cell Biol.* 3, 607–610.
33. Effler, J.C., Kee, Y.-S., Berk, J.M., Tran, M.N., Iglesias, P.A., and Robinson, D.N. (2006). Mitosis-specific mechanosensing and contractile protein redistribution control cell shape. *Curr. Biol.* 16, 1962–1967.
34. Weber, I., Gerisch, G., Heizer, C., Murphy, J., Badelt, K., Stock, A., Schwartz, J.-M., and Faix, J. (1999). Cytokinesis mediated through the recruitment of cortexillins into the cleavage furrow. *EMBO J.* 18, 586–594.
35. Robinson, D.N., Ocon, S.S., Rock, R.S., and Spudich, J.A. (2002). Dynactin is a novel actin bundling protein that localizes to dynamic actin structures. *J. Biol. Chem.* 277, 9088–9095.
36. Prassler, J., Stocker, S., Marriott, G., Heidecker, M., Kellermann, J., and Gerisch, G. (1997). Interaction of a Dictyostelium member of the plastin/fimbrin family with actin filaments and actin-myosin complexes. *Mol. Biol. Cell* 8, 83–95.
37. Wachsstock, D.H., Schwarz, W.H., and Pollard, T.D. (1994). Cross-linker dynamics determine the mechanical properties of actin gels. *Biophys. J.* 66, 801–809.
38. Rappaport, R. (1967). Cell division: Direct measurement of maximum tension exerted by furrow of echinoderm eggs. *Science* 156, 1241–1243.
39. Hiramoto, Y. (1990). Mechanical properties of the cortex before and during cleavage. *Ann. N Y Acad. Sci.* 582, 22–30.
40. Nagasaki, A., deHostos, E.L., and Uyeda, T.Q.P. (2002). Genetic and morphological evidence for two parallel pathways of cell-cycle-coupled cytokinesis in Dictyostelium. *J. Cell Sci.* 115, 2241–2251.
41. Yumura, S., and Fukui, Y. (1998). Spatiotemporal dynamics of actin concentration during cytokinesis and locomotion in *Dictyostelium*. *J. Cell Sci.* 111, 2097–2108.
42. Mukhina, S., Wang, Y.L., and Murata-Hori, M. (2007). Alpha-actinin is required for tightly regulated remodeling of the actin cortical network during cytokinesis. *Dev. Cell* 13, 554–565.
43. Humphrey, D., Duggan, C., Saha, D., Smith, D., and Kas, J. (2002). Active fluidization of polymer networks through molecular motors. *Nature* 416, 413–416.
44. Lele, T.P., Pendse, J., Kumar, S., Salanga, M., Karavitis, J., and Ingber, D.E. (2006). Mechanical forces alter zyxin unbinding kinetics within focal adhesions of living cells. *J. Cell. Physiol.* 207, 187–194.
45. Gerald, N., Dai, J., Ting-Beall, H.P., and DeLozanne, A. (1998). A role for Dictyostelium racE in cortical tension and cleavage furrow progression. *J. Cell Biol.* 141, 483–492.
46. Hochmuth, R.M. (2000). Micropipette aspiration of living cells. *J. Biomech.* 33, 15–22.
47. Evans, E., and Yeung, A. (1989). Apparent viscosity and cortical tension of blood granulocytes determined by micropipet aspiration. *Biophys. J.* 56, 151–160.
48. Yumura, S., Yoshida, M., Betapudi, V., Licate, L.S., Iwadata, Y., Nagasaki, A., Uyeda, T.Q., and Egelhoff, T.T. (2005). Multiple myosin II heavy chain kinases: Roles in filament assembly control and proper cytokinesis in Dictyostelium. *Mol. Biol. Cell* 16, 4256–4266.

Interactions between Myosin and Actin Crosslinkers Control Cytokinesis Contractility Dynamics and Mechanics

Elizabeth M. Reichl, Yixin Ren, Mary K. Morpew,
Michael Delannoy, Janet C. Effler, Kristine D. Girard,
Srikanth Divi, Pablo A. Iglesias, Scot C. Kuo
and Douglas N. Robinson

Supplemental Experimental Procedures

Cell Culture

Dictyostelium discoideum strains are presented in Table S1. Constructs were transformed into either the wild-type strain (Ax2 or Ax3:Rep orf+; HS1000) [S1], the myosin-II heavy chain null (*myoII*) strain (*mhcA*; HS1) [S2], or the *fimbrin* null strain (HG1629) and selected in 1.4× HL5 containing 8% FM (Enriched HL-5) and 15–30 µg/ml G418. Tubulin was observed by using pDXA-BI: RFP-tubulin or pDRH:GFP- or RFP-tubulin [S3].

To construct the *fimbrin* RNAi hairpin plasmid, unique regions of the gene that were not homologous to other genes were identified. The stem of the hairpin was constructed by cloning the antisense and sense sequences of the unique region in series. A loop region of ~500 nucleotides from the antisense sequence lies between the antisense and sense stem regions. Sequences that contributed to the stem region of the RNAi hairpin were blasted against the Dictybase, and it was determined that there are no stretches with ≥16 out of 20 base pair identities to genes other than those of interest, thus eliminating the possibility of nonspecific RNAi.

Altered *fimbrin* and myosin-II expression levels were determined by western analysis using a monoclonal anti-*fimbrin* 1° antibody [S4] or anti-myosin-II heavy chain 1° antibody, and a goat anti-mouse 2° antibody (Sigma). The protein concentrations were determined by Bradford (BioRad). Dilutions series of total protein in control and *fimbrin* strains were used to determine the fold reduction in *fimbrin* levels. Equal loading was confirmed using a polyclonal anti-dynactin 1° antibody [S5] and a donkey anti-rabbit 2° antibody.

Genetic Screen

A *D. discoideum* cDNA library prepared from vegetative cells was transformed into HS1000 cells as described previously [S5]. 37,000 transformants were screened visually for colonies with a large proportion of enlarged cells. Mutants were cloned and genes identified and recapitulated as described previously [S5].

Growth in Suspension

Log phase wt control and wt: *fimOE* strains were grown in suspension culture at an initial concentration of ~2 × 10⁵ cells/ml. Cell concentrations were determined using a hemacytometer.

Transmission and Scanning Electron Microscopy

Transmission electron microscopy (Pt-TEM) and scanning electron microscopy (Pt-SEM) were performed on wild-type and *myoII* mutant cells undergoing cytokinesis, using methods adapted from [S6]. Wild-type (Ax3:Rep orf+; pLD1A15SN) or *myoII* mutant cells were plated overnight on circular coverslips in enriched HL5 media and then fixed. After critical point drying, samples were platinum- or platinum/palladium-shadowed by using a Denton Vacuum DV-502A evaporator. Platinum shadowed coverslips were imaged by using a Zeiss LEO field emission scanning electron microscope operating at 1 keV. For Pt-TEM, platinum replicas of cells were transferred to parlodion-coated 200 mesh copper EM grids and then imaged with an AMT 1k × 1k CCD camera. Images were inverted to highlight actin filaments. Pt-TEM micrographs of cells showing the distinctive shape of cells undergoing cytokinesis were obtained using a Hitachi 7600 transmission electron microscope, operating at 80 keV.

3D Electron Tomography

To exclude the possibility that detergent-solubilization of the cell membrane disrupted furrow actin organization, 3D electron tomography was performed. Cells were grown on formvar-coated gold EM grids for 6–18 hr. Cells were rinsed in 1× phosphate buffered saline (PBS), blotted, and plunged into a reservoir of liquid ethane that was cooled to –180°C in a bath of liquid nitrogen. Frozen grids with cells were transferred to vials containing frozen freeze substitution fluid (1% OsO₄, 0.1% uranyl acetate in acetone).

Samples were warmed to –9°C and substituted at this temperature for 3 days, warmed to 0°C gradually over 24 hr, rinsed with acetone, and embedded in Epox-Araldite. Sections (300 nm) were cut by using an ultramicrotome (Leica Microsystems, Wein, Austria), collected on formvar-coated copper slot grids and post-stained with uranyl acetate and Reynold's lead citrate.

Serial tilted images were collected at 1° increments (±60°) around an orthogonal axis by using the program SerialEM [S7] on a Tecnai F30 electron microscope (FEI, Eindhoven, Netherlands) by using a Gatan CCD camera (Pleasanton, CA). The 3D density distributions (tomograms) calculated from each set of aligned tilts were aligned with each other and combined to produce a single, dual-axis 3D reconstruction. Structures within the volume of the tomographic reconstruction were modeled by using the IMOD software package [S8].

3D Deconvolution and Total Internal Reflection Fluorescence

To determine the organization of GFP-myosin-II and F-actin at the furrow, *myoII* null cells expressing GFP-myosin-II and GFP-tubulin were imaged. Cells were grown on coverslips for at least 1 hr prior to live-cell imaging and overnight before –20°C acetone fixation for actin staining. Cells were fixed for 3 min and then blocked in 1× PBT (1× PBS, 0.05% Triton X-100, and 0.5% BSA). After blocking, cells were stained for 3 hr in 40 nM TRITC-phalloidin + 1 µg/ml DAPI in 1× PBT. After extensive washing in 1× PBT and 1× PBS, coverslips were mounted in 90% glycerol 1× PBS. For live-cell fluorescence imaging, the media was replaced with MES buffer (50 mM MES [pH 6.8], 2 mM MgCl₂, 0.2 mM CaCl₂) to reduce auto-fluorescence. Z section micrographs throughout the cell volume were acquired by using an Olympus microscope and 60× (NA 1.45) objective with 1.6× optivar. Deconvolution of GFP-myosin-II and TRITC-phalloidin stained F-actin during cytokinesis was performed using Metamorph software (Molecular Devices). To quantify the concentration of F-actin at the furrow during different phases of cytokinesis, images were background subtracted by using a region outside of the cell, and then the mean fluorescence intensity of the furrow cortices of deconvolved TRITC-phalloidin stained cells were normalized to the mean fluorescence intensity of the cytoplasm. The section of the deconvolved images with the largest width was used for measurement of fluorescence intensities by using ImageJ software (<http://rsb.info.nih.gov/ij/>). Relative fluorescence intensities were calculated using Microsoft Excel. To plot the actin concentrations, the relative furrow diameter was calculated by dividing each cell's furrow width by the D_x of *myoII*:GFPmyoII cells (2.5 µm; Table S2) [S9]. To observe the organization of myosin-II thick filaments during cytokinesis, time-lapse total internal reflection fluorescence (TIRF) microscopy was performed using a 60× (NA 1.45) objective and a 488 nm laser.

Fluorescence Recovery after Photobleaching

To determine if GFP-tagging affected dynactin or *fimbrin* function, we used MPA to compare the effective tension (T_{eff}) of wild-type and *myoII* mutant control and *fimbrin* or dynactin overexpressing cells. In these MPA experiments, the wild-type control for Ax2:: pLD1A15SN:GFP-dynactin is Ax2-214 and the wild-type control for Ax3 Rep:orf+:: pLD1A15SN: *fimbrin* is Ax3 Rep:orf+:: pLD1A15SN. Like the non-tagged versions, GFP-dynactin and GFP-*fimbrin* overexpression increased the T_{eff} of cells over control (Figure S5) [S10].

For fluorescence recovery after photobleaching (FRAP) experiments, we used a Zeiss Meta confocal with a 63× objective and a 488 nm laser. Non-bleaching exposures of cells were performed at 10%–15% laser power. The interval between exposures was 200 ms for GFP-cortexillin-I or GFP-myosin-II expressing cells and 50 ms for GFP, GFP-*fimbrin*, or GFP-dynactin expressing cells. Bleaching of regions of interest (ROI) occurred at 100% laser power for 20 iterations and at the cortex for all FRAP measurements shown in Table 1. Fluorescence of bleached ROIs were background corrected and normalized to overall photobleaching due to laser exposures.

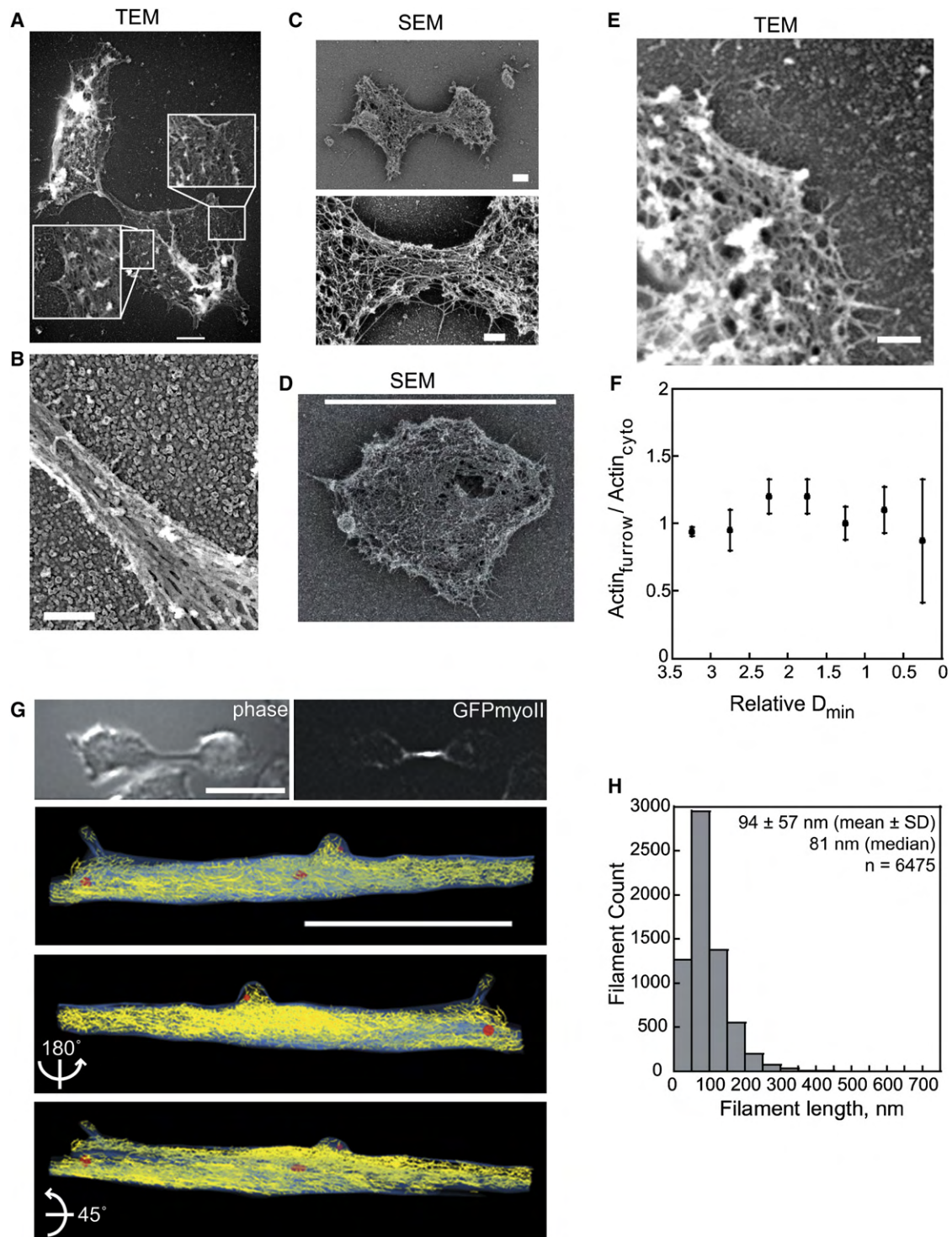


Figure S1. Organization and Quantification of Actin Cytoskeleton

(A) Pt replicas of a wild-type cell at a late stage of cytokinesis imaged BY using TEM. Insets show higher magnification views of the polar cortices. Scale bar, 2 μm .

(B) Zoom in of the bridge in (A). Scale bar, 500 nm.

(C) Scanning electron micrographs of a wild-type cell undergoing cytokinesis prior to fixation, membrane extraction, and metal shadowing. Scale bar, upper panel, 2 μm ; lower panel, 1 μm .

(D) Scanning electron micrograph of a wild-type interphase cell. Scale bar, 10 μm .

(E) Close-up view of a Pt replica of a region of the polar cortex of a dividing cell imaged by TEM. Scale bar, 500 nm.

(F) Quantification of the actin concentration at the furrow normalized to the concentration of the cytoplasm during cytokinesis and plotted versus the relative diameter (D_{\min}) normalized by D_x . A total of 56 cells were measured for the complete analysis.

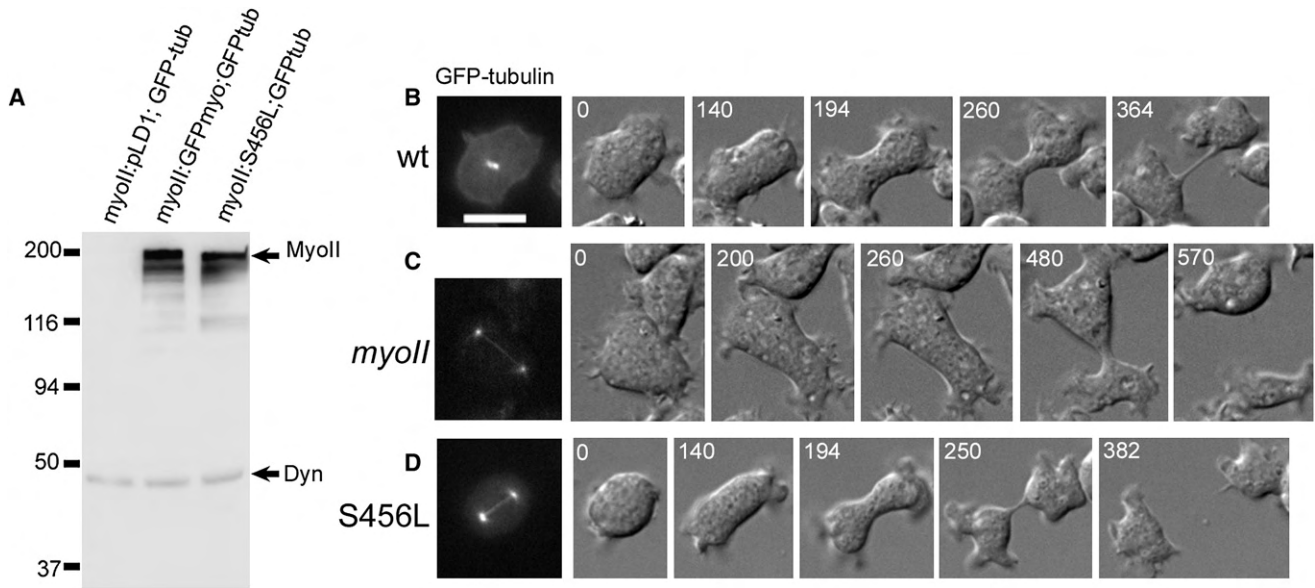


Figure S2. Myosin-II Dictates the Morphology of the Cleavage Furrow

(A) Western blot of myosin-II expression with dynactin as a loading control.

(B–D) Time series of wild-type (*myoII::GFPmyoII*), *myosin-II* control, and *myosin-II* cells expressing mutant myosin-II S456L undergoing cytokinesis. Each strain is expressing GFP-tubulin and the GFP image is shown, confirming that all cells are mitotic. Scale bar, 10 μ m and applies to all images. Corresponding movies are also presented (see Movies S3–S5).

The background fluorescence was accounted for by measuring a region outside of the cell and the photobleaching rate was determined by fitting the background corrected fluorescence of a non-bleached region of the cell to the equation:

$$F_{pb}(t) = a \times e^{-bt} + c \times e^{-dt}, \quad (1)$$

where $F_{pb}(t)$ = the fluorescence at time t . Data analysis was performed by using ImageJ (<http://rsb.info.nih.gov/ij/>), LSM browser, Microsoft Excel, Kaleidograph (Synergy Software, Reading, PA), and Matlab. Movement of cells during imaging was accounted for by using ImageJ's Turboreg plugin. Recovery times (τ_{rec}) were determined by fitting the recovery curve to the equation:

$$F(t) = f - g \times e^{-(t/\tau_{rec})}, \quad (2)$$

where $F_p(t)$ is the relative fluorescence of the normalized bleached ROI. Immobile fractions (F_i) were calculated by using the equation:

$$F_i = 1 - f / (1 - f + g). \quad (3)$$

For equatorial FRAP measurements, to ensure that we were still measuring fluorescence recovery that was not limited by transport of the proteins into the furrow region, we did not measure cells with furrows that were:

$$\frac{\text{Furrow width}}{\text{daughter cell width}} \leq 0.4. \quad (4)$$

Fluorescence Loss in Photobleaching

Fluorescence loss in photobleaching (FLIP) experiments were performed on interphase Ax2:: pLD1A15SN:GFP-dynactin; pDRH:RFP-tubulin and Ax3:Rep orf+ (HS1000):: pLD1A15SN:GFP-fimbrin; pDRH:RFP-tubulin cells. The cytoplasmic region internal to the cortex was bleached at 100% laser power for 20 iterations. To determine the fraction of fluorescence that remained at the cortex after bleaching, the ratio of the background corrected fluorescence at a region of the cortex post- and pre-bleach of the cytoplasm

was calculated. Photobleaching due to nonbleaching exposures at 10% laser power are negligible after 1 exposure.

Nuclei per Cell Distributions

To determine nuclei/cell distributions, log-phase Ax3:Rep orf+ (HS1000):: pLD1A15SN and Ax3:Rep orf+ (HS1000):: pLD1A15SN:fimbrin cells were grown, fixed, stained, and analyzed as previously described [S5].

Cellular Localization

Ax3:Rep orf+ (HS1000):: pLD1A15SN:GFP-fimbrin cells were imaged at 100 ms exposures in low-fluorescent media to decrease background fluorescence [S11]. Immunocytochemistry of Ax3:Rep orf+ (HS1000):: pLD1A15SN cells was performed by using a monoclonal anti-fimbrin 1° antibody [S4] and a FITC anti-mouse 2° antibody (Sigma).

Supplemental References

- S1. Robinson, D.N., Ocon, S.S., Rock, R.S., and Spudich, J.A. (2002). Dynactin is a novel actin bundling protein that localizes to dynamic actin structures. *J. Biol. Chem.* 277, 9088–9095.
- S2. Ruppel, K.M., Uyeda, T.Q.P., and Spudich, J.A. (1994). Role of highly conserved lysine 130 of myosin motor domain. In vivo and in vitro characterization of site specifically mutated myosin. *J. Biol. Chem.* 269, 18773–18780.
- S3. Effler, J.C., Kee, Y.-S., Berk, J.M., Tran, M.N., Iglesias, P.A., and Robinson, D.N. (2006). Mitosis-specific mechanosensing and contractile protein redistribution control cell shape. *Curr. Biol.* 16, 1962–1967.
- S4. Prassler, J., Stocker, S., Marriott, G., Heidecker, M., Kellermann, J., and Gerisch, G. (1997). Interaction of a Dictyostelium member of the plastin/fimbrin family with actin filaments and actin-myosin complexes. *Mol. Biol. Cell* 8, 83–95.
- S5. Robinson, D.N., and Spudich, J.A. (2000). Dynactin, a genetic link between equatorial contractility and global shape control discovered by library complementation of a Dictyostelium discoideum cytokinesis mutant. *J. Cell Biol.* 150, 823–838.

(G) Phase and fluorescence imaging of GFP-myosin-II in a wild-type cell prior to fixation and imaging by 3D-EM. Scale bar, 10 μ m. Model of 3D-EM imaged cell shows disordered actin filaments in the bridge. Three views are shown. Scale bar, 2 μ m. The corresponding movie is presented in Movie S2.

(H) The distribution of actin filament lengths determined from modeling of 3D-EM tomograms of the furrows of wild-type cells during cytokinesis.

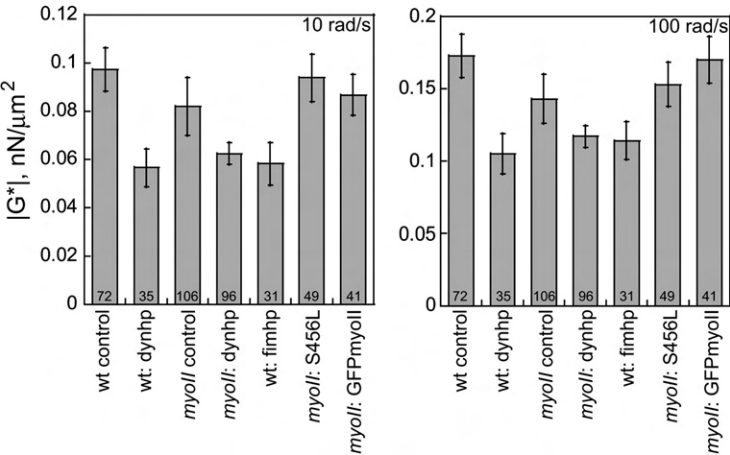


Figure S3. The Viscoelasticity $|G^*|$ Values at Specific Frequencies for Wild-Type Cells and Cells with Altered Dynacortin, Myosin-II and/or Fimbrin Expression
Values are present for sampling frequencies of 10 rad/s (100 ms) and 100 rad/s (10 ms). Error bars represent standard error of the mean after transformation of values from log space to real space.

S6. Svitkina, T.M., and Borisy, G.G. (1999). Arp2/3 and actin depolymerizing factor/cofilin in dendritic organization and treadmilling of actin filament array in lamellipodia. *J. Cell Biol.* 145, 1009–1026.

S7. Mastronarde, D.N. (2005). Automated electron microscope tomography using robust prediction of specimen movements. *J. Struct. Biol.* 152, 36–51.

S8. Kremer, J.R., Mastronarde, D.N., and McIntosh, J.R. (1996). Computer visualization of three-dimensional image data using IMOD. *J. Struct. Biol.* 116, 71–76.

S9. Zhang, W., and Robinson, D.N. (2005). Balance of actively generated contractile and resistive forces controls cytokinesis dynamics. *Proc. Natl. Acad. Sci. USA* 102, 7186–7191.

S10. Girard, K.D., Chaney, C., Delannoy, M., Kuo, S.C., and Robinson, D.N. (2004). Dynacortin contributes to cortical viscoelasticity and helps define the shape changes of cytokinesis. *EMBO J.* 23, 1536–1546.

S11. Nagasaki, A., deHostos, E.L., and Uyeda, T.Q.P. (2002). Genetic and morphological evidence for two parallel pathways of cell-cycle-coupled cytokinesis in Dictyostelium. *J. Cell Sci.* 115, 2241–2251.

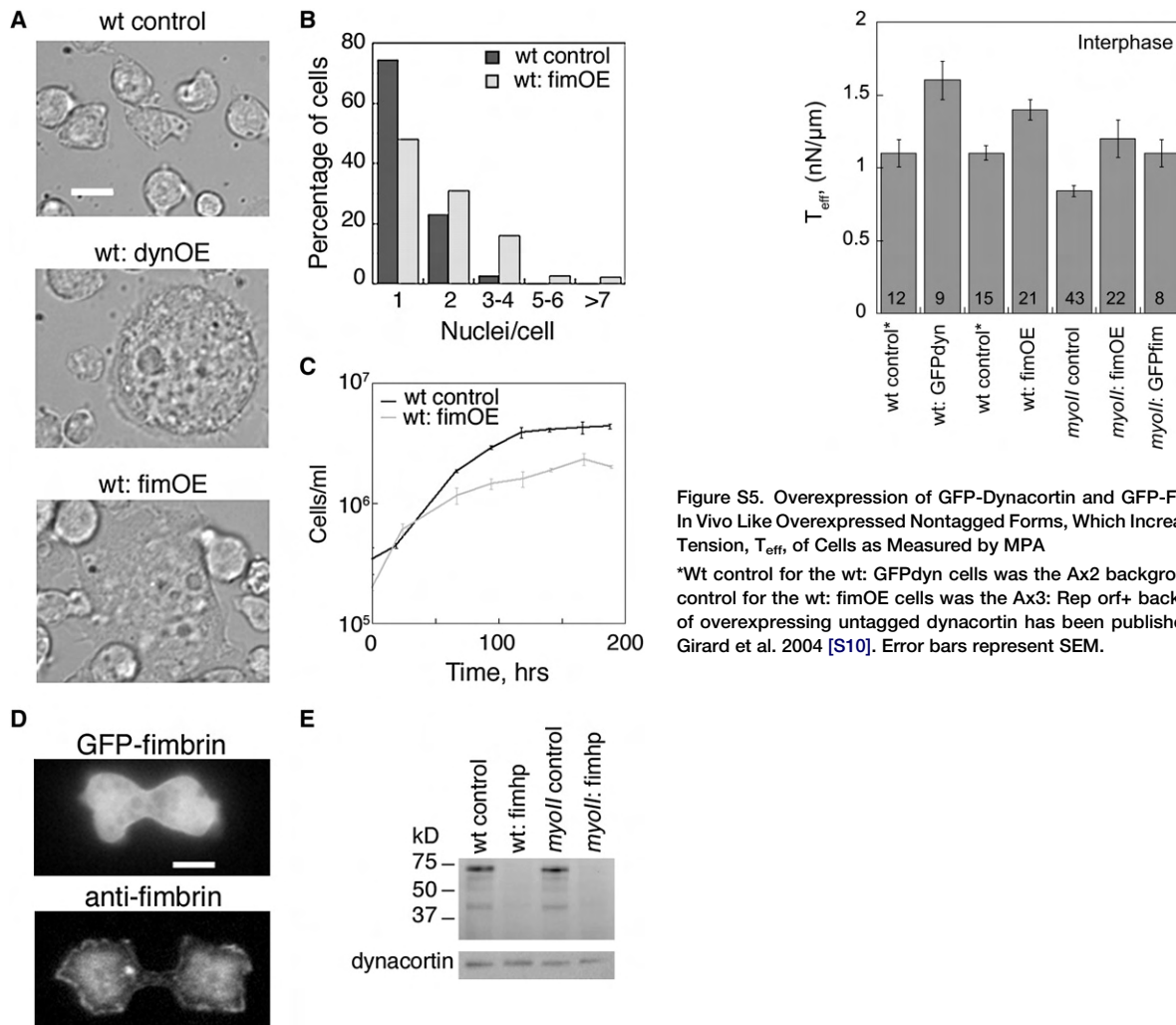


Figure S4. Fimbrin Is a Global Actin Crosslinker that Slows Cytokinesis Kinetics and, When Overexpressed, Inhibits Cytokinesis

(A) Like overexpression of the global actin crosslinker dynacortin, fimbrin overexpression leads to enlarged cells. Scale bar, 10 μ m and applies to all images.

(B) Overexpression of fimbrin (613 cells) increases multinucleation compared to wild-type cells (635 cells).

(C) Cell proliferation in suspension culture is inhibited by fimbrin overexpression. Error bars, SEM, $n = 3$.

(D) Fimbrin localizes to the global actin cortex. Scale bar, 10 μ m and applies to all images.

(E) Western blots of fimbrin RNAi in wild-type and myosin-II cells. Dynacortin is a loading control.

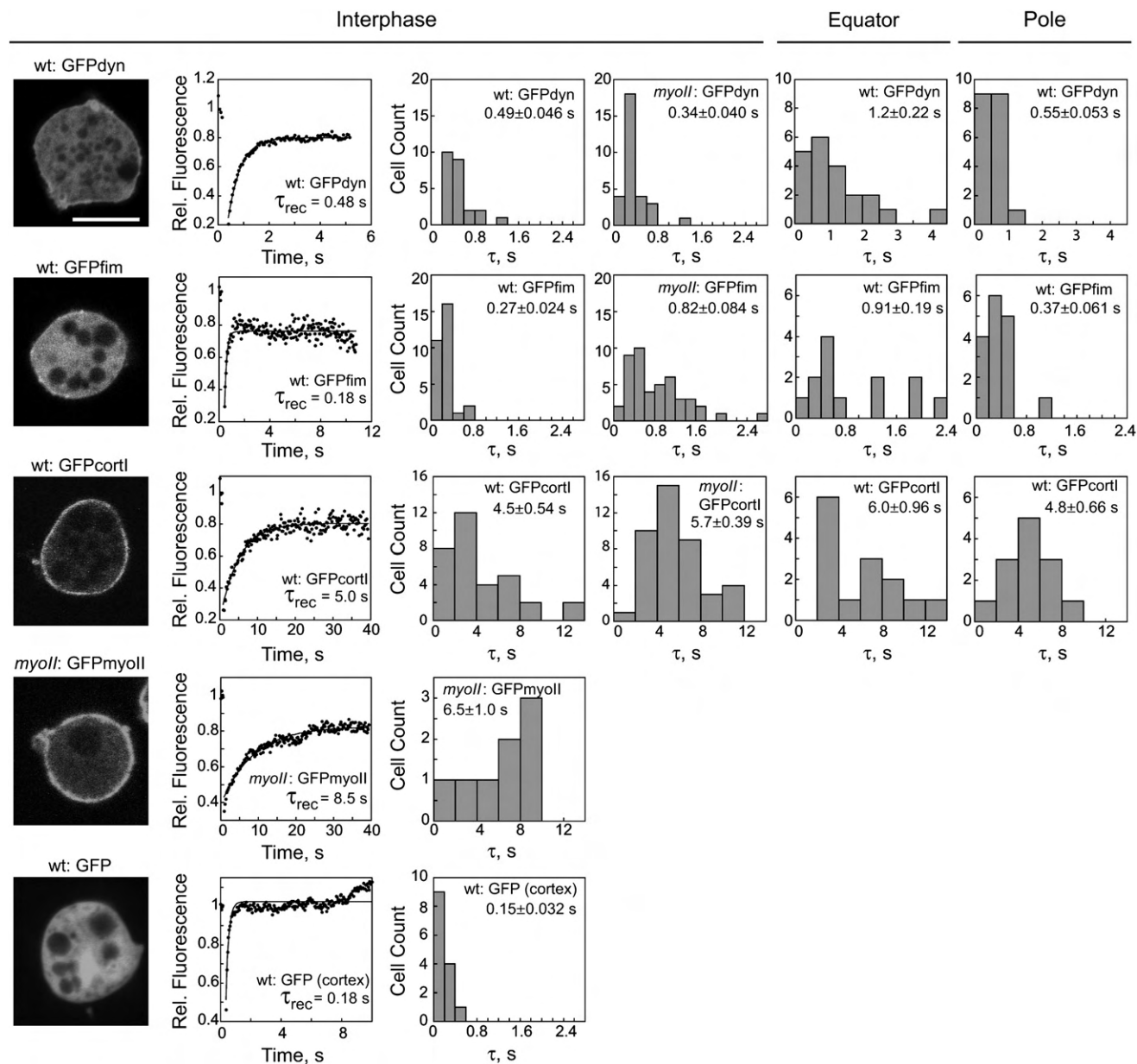


Figure S6. FRAP Analysis of Strains

Confocal images of cells expressing GFP-dynactin, GFP-fimbrin, GFP-cortillin-I, GFP-myosin-II, and soluble GFP during interphase. Scale bar, 10 μ m and applies to all images. Representative FRAP recovery curves and curve fits are shown. The distributions of τ_{rec} determined by fluorescence recovery after photo-bleaching (FRAP) measurements in wild-type and *myosin-II* strains during interphase and during wild-type cytokinesis are shown in histograms. Mean \pm SEM are shown on the histograms. Medians and sample sizes are shown in Table 1.

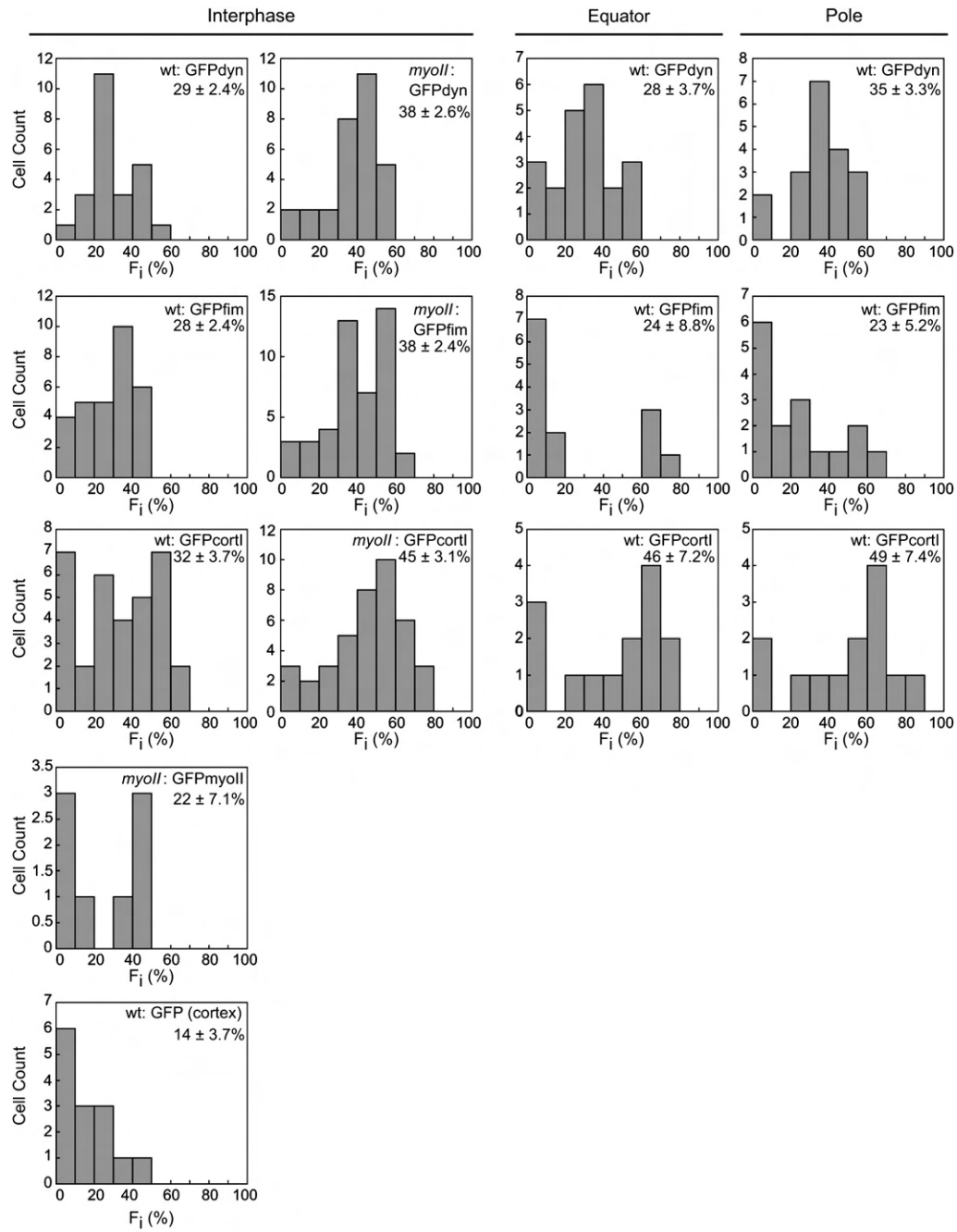


Figure S7. Frequency Distributions of Immobile Fractions from FRAP Analysis

Mean \pm SEM are shown on the histograms. These histograms correspond with the median values and sample sizes presented in Table 1. As a check, we also performed fluorescence loss in photobleaching (FLIP) analysis of GFP-dynacortin (median 19%, $n = 10$) and GFP-fimbrin (median 25%, $n = 11$) during interphase. These values agree well with the median values of 26% and 33% measured for these proteins, respectively, using FRAP (Table 1).

Table S1. Strains Used in This Study

Strain	Features	Experiment
wt control	Ax2-214	MPA
<i>fimbrin</i>	HG1629	MPA
wt control	Ax3:Rep orf+ (HS1000):: pLD1A15SN	TEM, MPA, LTM, genetic screen, suspension growth, DAPI, immunocytochemistry, western
wt: fimhp	Ax3:Rep orf+ (HS1000):: pLD1A15SN:fimbrin RNAi	MPA, LTM, western
wt: dynhp	Ax3:Rep orf+ (HS1000):: pLD1A15SN:dynacortin RNAi	MPA, LTM
wt: fimOE	Ax3:Rep orf+ (HS1000):: pLD1A15SN:fimbrin	Genetic screen, suspension growth, DAPI, MPA
wt: dynOE	Ax3:Rep orf+ (HS1000):: pLD1A15SN:dynacortin	Genetic screen
wt: GFP-fim	Ax3:Rep orf+ (HS1000):: pLD1A15SN:GFP-fimbrin	FRAP (Interphase)
wt: GFP-fim	Ax3:Rep orf+ (HS1000):: pLD1A15SN:GFP-fimbrin; pDRH:RFP-tubulin	FRAP (Cytokinesis), FLIP
wt: GFP-dyn	Ax3:Rep orf+ (HS1000):: pLD1A15SN:GFP-dynacortin	FRAP (Interphase)
wt: GFP-dyn	Ax2:: pLD1A15SN:GFP-fimbrin; pDRH:RFP-tubulin	FRAP (Cytokinesis), FLIP, MPA
wt: GFP-cortl	Ax3:Rep orf+ (HS1000):: pLD1A15SN:GFP-cortexillin-I	FRAP (Interphase)
wt: GFP-cortl	Ax3:Rep orf+ (HS1000):: pLD1A15SN:GFP-cortexillin-I; pDRH:RFP-tubulin	FRAP (Cytokinesis)
wt: GFP	Ax3:Rep orf+ (HS1000):: pLD1A15SN:GFP	FRAP
<i>myoII</i> control	<i>mhcA</i> (HS1):: pLD1A15SN	MPA, LTM, FTD, western
<i>myoII</i> control	<i>mhcA</i> (HS1):: pLD1A15SN; pDRH:GFP-tubulin	FTD
<i>myoII</i> : S456L	<i>mhcA</i> (HS1):: pBIG:S456L; pDRH:GFP-tubulin	FTD
<i>myoII</i> : S456L	<i>mhcA</i> (HS1):: pBIG:S456L	MPA, LTM
<i>myoII</i> : fimhp	<i>mhcA</i> (HS1):: pLD1A15SN:fimbrin RNAi	FTD, MPA, LTM, western
<i>myoII</i> : dynhp	<i>mhcA</i> (HS1):: pLD1A15SN:dynacortin RNAi	FTD, MPA, LTM
<i>myoII</i> : fimOE	<i>mhcA</i> (HS1):: pLD1A15SN:fimbrin	MPA
<i>myoII</i> : GFPmyoII	<i>mhcA</i> (HS1):: pBIG:GFP-myosin-II	LTM, FRAP
<i>myoII</i> : GFPmyoII	<i>mhcA</i> (HS1):: pBIG:GFP-myosin-II	LTM
<i>myoII</i> : GFPmyoII	<i>mhcA</i> (HS1):: pBIG:GFP-myosin-II; pDRH:RFP-tubulin	3D-EM, MPA
<i>myoII</i> : GFPmyoII	<i>mhcA</i> (HS1):: pBIG:GFP-myosin-II; pDRH:GFP-tubulin	3D-decon, TIRF, FTD
<i>myoII</i> : GFP-fim	<i>mhcA</i> (HS1):: pLD1A15SN:GFP-fimbrin	FRAP, MPA
<i>myoII</i> : GFP-dyn	<i>mhcA</i> (HS1):: pLD1A15SN:GFP-dynacortin	FRAP
<i>myoII</i> : GFP-cortl	<i>mhcA</i> (HS1):: pLD1A15SN:GFP-cortexillin-I	FRAP

Table S2. D_x Values of Furrow-Thinning Dynamics Trajectories

Strain	D_x	n
Values for Figure 2A		
<i>myoII</i> :GFPmyoII; GFP-tubulin	2.5 ± 0.16	8
<i>myoII</i> control: GFP-tubulin	1.9 ± 0.14	5
<i>myoII</i> :S456L; GFP-tubulin	2.2 ± 0.18	19
Values for Figure 3E		
<i>myoII</i> control	1.9 ± 0.087	27
<i>myoII</i> : dynhp*	2.4 ± 0.12	15
<i>myoII</i> : fimhp	1.8 ± 0.12	14

*Data for *myoII*:dynhp is reproduced from Zhang and Robinson, 2005 [S9].

Table S3. Elastic Moduli, E, and Number of Cells Measured for ΔP versus L_p/R_p Plots in Figure 2

Strain	E, nN/ μm^2 (Total number of measurements/Total number of Cells)			
	Interphase	Metaphase	Furrow	Pole
Wild-type control	0.095 (20/20)	—	—	—
<i>myoII</i> :GFPmyoII	0.10 (25/25)	0.10 (13/8)	0.13 (18/12)	0.12* (19/14)
<i>myoII</i> :S456L	0.075 (20/20)	—	0.13 (13/8)	0.084* (36/24)
<i>myoII</i> control	0.095* (20/20)	—	0.075* (25/19)	0.054* (16/15)

*Note that these strains show offsets, which may reflect nonlinear responses to the applied pressure.